Available online at www.sciencedirect.com

ScienceDirect

www.elsevier.com/locate/jmbbm

Structural modifications induced by compressive plastic deformation in single-step and sequentially irradiated UHMWPE for hip joint components

Leonardo Puppulin[a,*], *Nobuhiko Sugano*[b], *Wenliang Zhu*[b], *Giuseppe Pezzotti*[a,c]

[a]*Ceramic Physics Laboratory and Research Institute for Nanoscience, Kyoto Institute of Technology, Sakyo-ku, Matsugasaki, 606-8585 Kyoto, Japan*
[b]*Department of Orthopedic Surgery, Osaka University Medical School, 2-2 Yamadaoka, Suita 565-0871 Osaka, Japan*
[c]*The Center for Advanced Medical Engineering and Informatics, Osaka University,Yamadaoka, Suita, 565-0871 Osaka, Japan*

ARTICLE INFO

Article history:
Received 10 December 2012
Received in revised form
21 February 2013
Accepted 25 February 2013
Available online 20 April 2013

Keywords:
UHMWPE
Cross-linking
Hip arthroplasty
Raman spectroscopy
Compressive plastic deformation
Orientation distribution function

ABSTRACT

Structural modifications were studied at the molecular scale in two highly crosslinked UHMWPE materials for hip-joint acetabular components, as induced upon application of (uniaxial) compressive strain to the as-manufactured microstructures. The two materials, quite different in their starting resins and belonging to different manufacturing generations, were a single-step irradiated and a sequentially irradiated polyethylene. The latter material represents the most recently launched gamma-ray-irradiated polyethylene material in the global hip implant market. Confocal/polarized Raman spectroscopy was systematically applied to characterize the initial microstructures and the microstructural response of the materials to plastic deformation. Crystallinity fractions and preferential orientation of molecular chains have been followed up during *in vitro* deformation tests on unused cups and correlated to plastic strain magnitude and to the recovery capacity of the material. Moreover, analyses of the *in vivo* deformation behavior of two short-term retrieved hip cups are also presented. Trends of preferential orientation of molecular chains as a function of residual strain were similar for both materials, but distinctly different in their extents. The sequentially irradiated material was more resistant to plastic deformation and, for the same magnitude of residual plastic strain, possessed a higher capacity of recovery as compared to the single-step irradiated one.

1. Introduction

The functionality of acetabular components made of polyethylene in hip prostheses mainly includes shock protection/absorption, and displacement adjustments during gait motion, including mal-alignments and rotational strains. While fulfilling such critical tasks, the material might undergo serious morphological changes and structural modifications, usually a combination of creep and wear deformation (Dumbleton, 2002; Haraguchi et al., 2001; McDonald et al., 1995; Morscher et al., 1982). Such combined effects progress with clinical use, leading to an increased penetration of the femoral counterpart (also referred to as "migration" of the femoral head) and to the generation of microscopic wear debris. Extensive wear and/or creep of the acetabular component will necessary lead to the need of

*Corresponding author. Tel:+81 0757247568.
E-mail address: puppulin@chem.kit.ac.jp (L. Puppulin).

1751-6161/$ - see front matter © 2013 Elsevier Ltd. All rights reserved.
http://dx.doi.org/10.1016/j.jmbbm.2013.02.019

revision surgery (James et al., 1993; Oparaugo et al., 2001; Zhu et al., 2001). Since the early 1990s, mitigation of wear volume has been identified as a priority achievement to improve the *in vivo* performance of ultra-high molecular weight polyethylene (UHMWPE) for orthopedic application. Highly irradiated polyethylene was introduced for such purpose during the 1970s in Japan by Oonishi and, separately, by Grobbelaar in South Africa (Oonishii et al., 2000; Grobbelaar et al., 1978). However, a complete understanding of the role of cross-linking in reducing wear was only achieved by later studies (Wang et al., 1996; McKellop et al., 1999) and included manufacturing solutions to the problem of residual free radicals left in the material after the irradiation process through a post-irradiation annealing or melting step to eliminate free radicals (Moratoglu et al., 1999, 2001; McKellop et al., 1999). On the other hand, as far as creep deformation is concerned, clinical and retrieval studies have clarified that the linear migration rate of the femoral head could be high in the initial post-operative period, but it reduces significantly in subsequent years. Dai et al. (2000) reported linear migrations of 40% of the total penetration at a 10-year follow-up after 2 postoperative years. Femoral head migration after a mean evaluation time of 3~4 months represented 56% of the 2-year total, indicating the occurrence of significant creep displacements during the initial post-operative period. Clinical and simulator studies of cross-linked polyethylene liners also revealed high rates of penetration over the first 18 months or 1.5 million cycles, followed by significantly lower rates (Wroblewski et al., 1996). Numerous other reports (Devane et al., 1999; Isaac et al., 1996; Pedersen et al., 2001; Sychterz et al., 1999) showed consistent results, according to which, after the occurrence of an initial migration typically ranging from 0.2 to 0.4 mm, the subsequent penetration rate becomes very small. From a mechanistic viewpoint, one could regard femoral-head migration as a "natural" event of strain-energy minimization. In fact, creep of the liner would increase joint contact area and thus decrease contact pressures (i.e., perhaps also playing a role in the reduced penetration rate observed over time). However, in presence of a significant amount of dimensional changes due to creep, it is imperative to more accurately rationalize migration data, to link them to wear rates, and to understand the effects of both design parameters and polyethylene microstructures on combined creep and wear of acetabular cups. Multi-scale models can be used to investigate polymers melt flow and to give a useful insight into creep and relaxation phenomena in viscoelastic materials, but although numerical simulations might be quick to perform, their results strongly depend on the constitutive law selected for describing creep behavior (Maxian et al., 1996a, 1996b; Teoh et al., 2002). Moreover, they provide no physical insight into the role of the material microstructure on the deformation behavior, thus leaving the investigators with a merely phenomenological knowledge. This is an unsatisfactory situation, which not only hinders further phenomenological clarifications but also delay progresses in the microstructural design of biomedical polyethylene.

The main purpose of this paper is to judge about the creep resistance of differently manufactured hip cups and to investigate and compare the microstructural modifications induced by plastic compressive strain in commercially available UHMWPE materials belonging to two successive manufacturing generations. We use confocal Raman spectroscopy (Kumakura et al., 2009; Pezzotti et al., 2007, 2011, 2011b; Takahashi et al., 2010) to link microstructural changes to mechanical creep displacements, which represent the physical origin of femoral-head migration *in vivo*. This study builds upon the large body of information available from polymer physics about chain displacements under static loading (Roe, 1964; Yang et al., 2001) and represents a comparative benchmark test for evaluating the latest improvements made in the development of new polyethylene microstructures in the field of artificial hip joints. Limitations to the outputs of the present study should consist in the fact that the data obtained in the present creep experiments are not comprehensive of the environmental effects occurring in the human hip joint; neither dynamic fatigue issues have been taken into consideration here. Within such limitations, however, the presented data clearly clarify the differences in the intrinsic resistance to time-dependent plastic strain of the investigated acetabular cups and the physical reasons behind their different microstructural response to deformation.

2. Materials and methods

2.1. *Investigated pristine and retrieved samples*

Two UHMWPE acetabular liners have been analyzed, which differed both for their starting resins (including molecular weight and manufacturing process) and for the respective manufacturing procedures. Both types of component were manufactured by Stryker Orthopedics, Inc., Mahwah, NJ, USA. One type belonged to a former generation of polyethylene, the so-called brand Crossfire™, which was clinically introduced in 1998. Manufacturing of this material started from GUR 1050 extruded rods, which were gamma-irradiated in a single step with a nominal dose of 75 kGy, and subsequently annealed at 130 °C for 8 h. After being machined into the morphology of a liner and barrier packaged, the components were again exposed to gamma irradiation for sterilization purposes with the nominal dose of 30 kGy in nitrogen atmosphere. The newest liner generation studied was the brand X3™, which was clinically introduced in the Trident and Tritanium acetabular cup designs in 2005. Manufacturing of this latter material started from GUR 1020 compression-molded sheets, which were gamma irradiated at the nominal dose of 30 kGy and then annealed at 130 °C. The same procedure was sequentially repeated for three times (i.e., for a cumulative radiation dose of 90 kGy). Table 1 summarizes the differences in the starting resins and the different processing procedures followed for manufacturing the two types of investigated UHMWPE liner. In the case of analyses of as-received components, spectroscopic data were collected on three different samples for each type of liner, as explained in the following section.

Two short-term acetabular cup retrievals could be obtained from Osaka University Hospital and were investigated immediately after their respective revision surgeries in comparison with pristine unused samples of the same types.

Table 1 – Characteristics of the staring resins and salient details of the manufacturing procedures for Crossfire™ and X3™ liners.

	Crossfire™	X3™
Resin	GUR1050	GUR1020
Average molecular weight	$5.5–6 \times 10^6$ g/mol	3.5×10^6 g/mol
Process of consolidation	Ram extrusion	Compression molding
Irradiation	75 kGy Gamma ray	30 kGy in 3 steps (total 90 kGy)
Post-irradiation heat treatment	Annealing (130 °C for 8 h)	Annealing after each step (130 °C for 8 h)
Sterilization	30 kGy Gamma ray in nitrogen	Gas plasma
Crosslinking density*	0.11 ± 0.02 mol dm^{-3}	0.17 ± 0.02 mol dm^{-3}

* Wang et al., 2006.

Table 2 – Clinical data for the two short-term UHMWPE retrievals analyzed in this study.

	Patient	Follow-up	Cause of revision	Femoral head	Operative procedure
Retrieval #1 (CrossfireTM)	Male (68 year old)	7 months	Dislocation	32 mm CoCr	Cementless THA
Retrieval #2 (X3TM)	Male (77 year old)	3 months	Infection	44 mm CoCr	Cementless THA

One cup (referred to as Retrieval #1, henceforth) was of the Crossfire™ type and was implanted in the patient's body for 7 months. Another cup (referred to as Retrieval #2, henceforth) was of the X3™ type and was implanted in the patient's body for only 3 months. In both cases, the total hip replacement was made with using a cementless stem. The clinical data and other clinical characteristics of the two retrievals are summarized in Table 2.

2.2. *Mechanical deformation and spectroscopic procedures*

UHMWPE exhibits both viscous and elastic characteristics when undergoing deformation during implantation. For characterizing time-dependent deformations of rigid plastic materials in which also strain recovery takes place in a non-negligible amount (i.e., like the case under investigation), uniaxial relaxation tests (rather than creep tests under a constant load) in a compressive geometry best suite quantitative characterizations of residual strain. In these tests, a residual plastic deformation is induced in samples obtained from unused liners and the effect of strain recovery is also introduced by letting the compressively deformed sample unloaded for a sufficiently long time before spectroscopic evaluation. In our calibration experiments, samples were cut from the acetabular cups as received from the maker (Fig. 1a) into rectangular prisms $4 \times 4 \times 6$ mm in dimension (Fig. 1b). The area from which the samples were extracted corresponded to the zone of the acetabular cup that would correspond to the main wear zone when the cup is implanted. Particular care was taken in order to smooth down by polishing the areas immediately neighboring the four corners of the concave surface of the sample (cf. Fig. 1b), which enabled us to obtain a flat face of the sample, but also to preserve the original surface of the liner in the central area. This latter area was analyzed by means of Raman spectroscopic techniques, as explained later. In one-dimensional relaxation tests, performed by means of a uniaxial compressive jig already described in some of our previous papers (Kumakura et al., 2009; Pezzotti et al., 2011; Puppulin et al., 2011b) the material was subjected to a sudden compressive strain of a predetermined magnitude, which was kept constant for 24 h in order to allow the full occurrence of stress relaxation possible in the microstructure. The strain field was then released and the sample allowed recovering of its anelastic strain for additional 24 h, in order to obtain nearly full recovery, especially at low and moderate levels of deformation, as in the case of the present experiments (Bartczak et al., 1992b; Meyer and Pruitt, 2001). The applied force was measured by means of a uniaxial load cell attached to the head of the loading system and monitored throughout all the loading period. Compression test calibrations were repeated for each type of investigated material. Compressive load was applied stepwise. The residual (plastic) strain was measured along the sample long axis by means of a micrometer caliper, and the deformed samples analyzed by Raman spectroscopy. Spectroscopic characterizations served to analyze the modifications induced by compressive strain on the as-received microstructural assembly of the acetabular components, phenomenologically reproducing the compressive strain conditions encountered during *in vivo* loading. The experimental program carried out in this study was conceived based on the understanding that the creep displacements observed upon compressive loading should mainly depend on the initial degree of crystallinity and by chain mobility (i.e., in turn governed by the degree of cross-linking). Molecular displacements should, at relatively low deformation levels, physically depend on chain mobility, which thus we quantitatively monitored by polarized Raman spectroscopy.

Raman spectra were collected with a triple monochromator spectrometer (T-64000, ISA Jobin-Ivon/Horiba Group, Tokyo, Japan, grating 2400 gr/mm, spectral resolution of 0.02 cm^{-1}) equipped with a charge-coupled detector (i.e., a high-resolution CCD camera). The laser power at the UHMWPE surface was typically about 90 mW. The laser excitation source was a monochromatic blue line emitted by an Ar-ion laser at a wavelength of 488 nm. Spectral

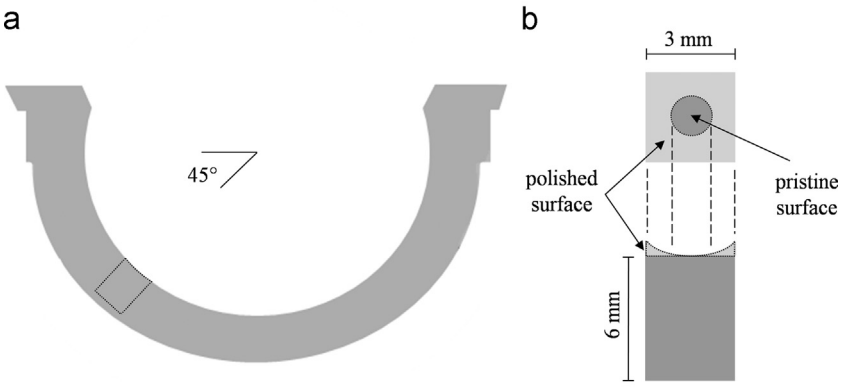

Fig. 1 – (a) Draft of the sample cutting procedure from acetabular cups as received from the maker; (b) rectangular prisms 4 × 4 × 6 mm in dimension used for uniaxial relaxation tests in compression.

integration times were typically 5 and 15s for unpolarized and polarized spectra, respectively. Each recorded spectrum was averaged over three successive measurements at each selected location. All Raman spectra were recorded at room temperature. Intensity and full width at half maximum (FWHM) of the 1130 cm^{-1} Raman band were retrieved by fitting the CCD raw data to mixed Gaussian/Lorentzian curves with commercially available software (Labspec, Horiba Co., Kyoto, Japan). Deformed UHMWPE samples were investigated by a confocal Raman probe (pinhole aperture 100 μm) at successive levels of deformation. For each type of polyethylene, the results of confocal Raman assessments were averaged on three different samples loaded to achieve the same deformation displacements. In the case of FWHM assessments, we used unpolarized Raman spectra. Microstructural modifications induced by uniaxial plastic strain were monitored at a depth of 50 μm below the surface of each sample. In band-width/strain calibration, an automated sample stage with sub-micrometric step precision was employed to collect square maps. The typical map size was 500 × 500 μm with a square mesh of 50 μm steps (for a total of 11 × 11=122 measurement points per each map). Therefore, for each step of deformation and type of polyethylene, the calculated FWHM was the average over 366 spectra.

In assessments of preferential molecular orientation and orientation distribution functions (ODF), confocal/polarized Raman spectra were collected at different azimuthal angles, ψ, using a rotating jig placed under the microprobe. In Fig. 2(a), a schematic draft is shown that explains the experimental set-up adopted for in-plane rotation assessments. Raman spectra were collected using sheet polarizers in parallel configuration with respect to the incident laser polarization vector. Particular care was taken in order to align the axis of the microscope with the axis of the rotation jig. For each point under investigation, Raman polarized spectra were collected at 19 different azimuthal angles within the interval $0^\circ \le \psi \le 180^\circ$, with sequential steps of 10°. Each data point in the plots of azimuthal angular dependencies shown in the remainder of this paper was calculated from a value averaged over twenty rotations performed at different locations of each deformed prismatic sample for each investigated strain value.

As far as spectroscopic analyses of retrievals were concerned, procedures similar to those described for the pristine samples were adopted, with the only difference that the samples were non-destructively analyzed. The main wear zone of each retrieved cup was investigated. The size of square maps (three for each retrieval) of unpolarized spectra for FWHM measurements was 50 × 50 μm with a square mesh of 2 μm steps (26 × 26=676 measurement points per collected map). In the case of molecular orientation and ODF analyses, parallel-polarized Raman spectra were collected upon in-plane rotation with sequential steps of 10°. The overall spectroscopic procedure was exactly the same as that used for deformation calibrations on pristine samples. Also in the case of the two analyzed retrievals, Raman assessments were made at a depth of 50 μm below the concave surface of the samples.

3. Theoretical background

3.1. *Molecular texture characterizations from polarized Raman spectra*

UHMWPE is a semicrystalline polymer in which a fraction of molecular chains rearranges into lamellar crystal embedded into an amorphous matrix. As far as the molecular orientation of the crystalline lamellae is involved, the tensorial rules governing the relative intensity of Raman bands for the orthorhombic crystal structure can be expressed into functions of Euler angles in space and probe polarization geometry (Loudon, 1964; Puppulin et al., 2011a; Turrell, 1989), by expanding the following tensorial equation:

$$I \propto |e_i \Re e_s|^2 \quad (1)$$

where I represents the scattered Raman intensity; e_i and e_s are the unit polarization vectors of the electric field for incident and scattered light, respectively. For a fixed polarization vector of the incident light (i.e., which is the case of our Raman equipment), two polarization geometries (i.e., parallel and cross) are possible for the scattered light. In the case of parallel polarization, which is the geometry adopted

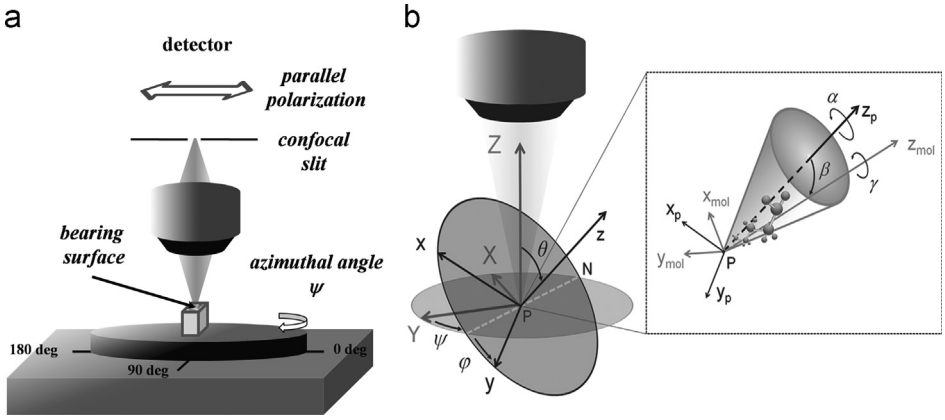

Fig. 2 – (a) Schematic draft of the experimental set-up adopted for in-plane rotation assessments. Raman spectra in parallel polarization configuration were collected at 19 different azimuthal angles within the interval $0^\circ \le \psi \le 180^\circ$, with sequential steps of 10°; (b) choice of Cartesian systems and sets of Euler angles as employed in the statistical determination of molecular textures according to the procedure described in Section 3.2.

in this study, the unit polarization vectors can be expressed in Cartesian coordinates, as follows:

$$e^{\parallel}_{i\,xyz} = (0 \quad 1 \quad 0), e^{\parallel}_{s\,xyz} = \begin{pmatrix} 0 \\ 1 \\ 0 \end{pmatrix} \tag{2}$$

where the subscripts i and s refer to incident and scattered light, respectively; the superscript ∥ indicates parallel polarization (i.e., $Z(YY)\bar{Z}$ in Porto notations (Porto and Krishnan, 1967)). $\mathfrak{R}$ represents the second-rank Raman scattering tensor of the vibrational mode under consideration. The Raman tensor expressed in the Cartesian frame of the principal crystal axis for the A_g and B_{1g} vibrational modesof an orthorhombic structure are given as (Loudon, 1964)

$$\mathfrak{R}_{A_g} = \begin{pmatrix} a & 0 & 0 \\ 0 & b & 0 \\ 0 & 0 & c \end{pmatrix}, \mathfrak{R}_{B_{1g}} = \begin{pmatrix} 0 & d & 0 \\ d & 0 & 0 \\ 0 & 0 & 0 \end{pmatrix} \tag{3}$$

A full expansion of Eq. (1) in the case of UHMWPE has been previously published (Takahashi et al., 2010). For brevity's sake, the procedure is not repeated here and only a brief description is given, which suffices for the present purpose. The preferential orientation of polyethylene molecules have been evaluated by analyzing the Raman band located at 1130 cm^{-1}, which is related to the C–C stretching vibration (A_g+B_{1g} mode). Rearranging from Eqs. (1)–(3), the dependence of Raman intensity on crystallographic orientation in parallel polarization can be explicitly expressed in terms of three Euler angles in space after rotation of the Cartesian frame, as follows (Puppulin et al., 2011b):

$$\begin{aligned} I^{\parallel}_{A_g+B_{1g}} = \Lambda\{ & \alpha[c\sin^2\theta\sin^2\psi + a(\sin\varphi\cos\psi + \cos\theta\cos\varphi\sin\psi)^2 \\ & + b(\cos\varphi\cos\psi - \cos\theta\sin\varphi\sin\psi)^2]^2 + (1-\alpha)[-2d(\sin\varphi\cos\psi \\ & + \cos\theta\cos\varphi\sin\psi)(\cos\varphi\cos\psi - \cos\theta\sin\varphi\sin\psi)]^2\} + \Gamma \end{aligned} \tag{4}$$

In Eq. (4), Λ and Γ represent numerical constants that depend on the instrumental configuration and on the spectral band employed; α is a fitting parameter that takes into account the contribution of A_g mode to the observed Raman band and it is also related to the orientation of the molecular chains. The Raman tensor parameters for A_g and B_{1g} modes assigned to the 1130 cm^{-1} Raman band (a=0.26, b=0.202, c=−0.898 and d=−0.67) have been determined in previous papers (Puppulin et al., 2011a; Takahashi et al., 2010). It should be noted that the application of Eqs. (1) and (4) in Raman analysis is straightforward only in the case of a complete or nearly complete alignment of fully crystalline microstructures (e.g., polyethylene fibers (Puppulin et al., 2011a)). On the other hand, a more comprehensive approach is needed to describe partly aligned/crystalline microstructures, like in the case of bulk polyethylene samples, because distributions of Euler angles are involved with the molecular arrangement in the microstructure. Accordingly, in order to obtain a fully quantitative assessment of the stereological character of UHMWPE molecular textures, an additional characterization of the statistical distribution of Euler angles at which the molecular chains are oriented is mandatorily needed. A method for assessing such statistical distributions is presented in the next section and applied in Section 4.1.

3.2. *Statistical distribution of molecular texture from in-plane rotational Raman characterizations*

Local orientation distribution functions (ODF) can be introduced in the computational routine, which statistically characterize the stereological orientation in space of polyethylene molecular chains. The structure of the ODF has been formulated in terms of Wigner functions using a formalism of polynomial expansion in series of Legendre (Citra et al., 1995; Nikolaeva et al., 1997; Pérez et al., 2008; Pigeon et al., 1991). Fig. 2(b) shows our choices of Cartesian systems, as follows: a Cartesian system (XYZ) fixed with respect to the laboratory, a Cartesian system (xyz) fixed with respect to the molecular orientation axes (i.e., with its z-axis parallel to the long axis of the molecular chain), and an additional Cartesian system ($x_{mol}y_{mol}z_{mol}$) locating the molecular orientation axes within the polarized Raman probe. The axes of preferential (average) orientation of the molecular structure were labeled as ($x_py_pz_p$), with z_p corresponding to the c-axis of the orthorhombic molecular frame. As far as different sets of Euler angles are concerned (i.e., as shown in Fig. 2(b)), the set of angles (θ, φ, ψ)

locates the orientation in space of an arbitrary polyethylene molecule (i.e., located by (xyz)) with respect to the Cartesian system (XYZ); the set of angles (α, β, γ) instead describes the rotations in space of the Cartesian frame fixed with respect to the molecular orientation axes, ($x_{mol}y_{mol}z_{mol}$), within the polarized Raman probe, with respect to the axes of preferential orientation of the molecular structure, ($x_py_pz_p$). In addition, the set of Euler angles describing the rotations of the preferential orientation axes, ($x_py_pz_p$), of the molecular chains with respect to the laboratory frame (XYZ) were labeled as (θ_p, φ_p, ψ_p). According to the above notations, the set of three Euler angles (θ, φ, ψ) describing the orientation of any arbitrary molecule in space with respect to the laboratory Cartesian system, (XYZ), can be expressed as functions of α, β, θ_p, φ_p and ψ_p by considering the following rotation matrices:

$$S=\begin{pmatrix} \cos\theta\cos\varphi\cos\psi-\sin\varphi\sin\psi & \cos\varphi\sin\psi+\cos\theta\cos\psi\sin\varphi & -\sin\theta\cos\psi \\ -\cos\theta\cos\varphi\sin\psi-\cos\psi\sin\varphi & \cos\varphi\cos\psi-\cos\theta\sin\varphi\sin\psi & \sin\theta\sin\psi \\ \sin\theta\cos\varphi & \sin\theta\sin\varphi & \cos\theta \end{pmatrix} \quad (5)$$

$$M=\begin{pmatrix} \cos\theta_p\cos\varphi_p\cos\psi_p-\sin\varphi_p\sin\psi_p & \cos\varphi_p\sin\psi_p+\cos\theta_p\cos\psi_p\sin\varphi_p & -\sin\theta_p\cos\psi_p \\ -\cos\theta_p\cos\varphi_p\sin\psi_p-\cos\psi_p\sin\varphi_p & \cos\varphi_p\cos\psi_p-\cos\theta_p\sin\varphi_p\sin\psi_p & \sin\theta_p\sin\psi_p \\ \sin\theta_p\cos\varphi_p & \sin\theta_p\sin\varphi_p & \cos\theta_p \end{pmatrix} \quad (6)$$

$$N=\begin{pmatrix} \cos\beta\cos\gamma\cos\alpha-\sin\gamma\sin\alpha & \cos\gamma\sin\alpha+\cos\beta\cos\alpha\sin\gamma & -\sin\beta\cos\alpha \\ -\cos\beta\cos\gamma\sin\alpha-\cos\alpha\sin\gamma & \cos\gamma\cos\alpha-\cos\beta\sin\gamma\sin\alpha & \sin\beta\sin\alpha \\ \sin\beta\cos\gamma & \sin\beta\sin\gamma & \cos\beta \end{pmatrix} \quad (7)$$

where $S=s_{ij}$ (i,j=1,2,3) represents the rotations of (xyz) with respect to (XYZ), $M=m_{ij}$ (i,j=1,2,3) the rotations of ($x_py_pz_p$) with respect to (XYZ), and $N=n_{ij}$ (i,j=1,2,3) the rotations of ($x_{mol}y_{mol}z_{mol}$) with respect to ($x_py_pz_p$) (cf. Fig. 2b). The matrix product $T=MN=t_{ij}$ (i,j=1,2,3) results equal to S. Thus, equating the elements $s_{33}=t_{33}$ and $s_{23}=t_{23}$, two Euler angles can be expressed as $\theta=\theta(\alpha, \beta, \theta_p, \varphi_p, \psi_p)$ and $\psi=\psi(\alpha, \beta, \theta_p, \varphi_p, \psi_p)$, as follows:

$$\theta=arccos(cos\beta cos\theta_p-cos(\alpha+\varphi_p)sin\beta sin\theta_p) \quad (8)$$

$$\psi=\arcsin\left\{\frac{\left[\begin{array}{l}\cos\alpha\cos\psi_p\sin\beta\sin\varphi_p+\sin\psi_p\left(\cos\beta\sin\theta_p-\cos\theta_p\sin\alpha\sin\beta\sin\varphi_p\right)\\ +\cos\varphi_p\sin\beta\left(\cos\psi_p\sin\alpha-\cos\alpha\cos\theta_p\sin\psi_p\right)\end{array}\right]}{\sqrt{1-\left(\cos\beta\cos\theta_p-\cos\left(\alpha+\varphi_p\right)\sin\beta\sin\theta_p\right)^2}}\right\} \quad (9)$$

Upon considering φ as a constant equal to φ_p in our calculations, namely neglecting any torsional rotations of the molecular chains around their c-axis, a working equation that includes both Raman selection rules and molecular distribution patterns can be set, as follows (Puppulin et al., 2011b):

$$I^{||}_{exp}(\theta,\varphi,\psi)=\frac{\int_{\gamma=0}^{\gamma=2\pi}\int_{\alpha=0}^{\alpha=2\pi}\int_{\beta=0}^{\beta=2\pi} I^{||,}_{A_g+B_{1g}}(\theta,\varphi,\psi)f(\beta)\sin\beta d\beta d\alpha d\gamma}{\int_{\gamma=0}^{\gamma=2\pi}\int_{\alpha=0}^{\alpha=2\pi}\int_{\beta=0}^{\beta=2\pi} f(\beta)\sin\beta d\beta d\alpha d\gamma} \quad (10)$$

with the polarized Raman intensity, $I^{||}_{A_g+B_{1g}}(\theta,\varphi,\psi)$, given by Eq. (4). The orientation distribution function, $f(\beta)$, can then be set as (Citra et al., 1995; Nikolaeva et al., 1997; Pérez et al., 2008; Pigeon et al., 1991):

$$f(\beta)=Aexp-[\lambda_2P_2(\cos\beta)+\lambda_4P_4(\cos\beta)] \quad (11)$$

where A is a constant and the parameters λ_2 and λ_4 are the Lagrange multipliers used in the definition of the principle of maximum information entropy reported by Jaynes (1957) and Pérez et al. (2008). Note that in the computational process, we excluded in first approximation any azimuthal dependence of the orientation distribution function, which is thus taken only dependent on the polar angle, β (i.e., assuming the existence of an uniaxial symmetry with respect to the preferential orientation of the molecular chains). Experimental Raman intensities collected upon in-plane rotation of the probe volume enable to set Eq. (10) (i.e., after substituting for the variables θ and ψ from Eqs. (8) and (9)) at each of n selected in-plane rotation angles, ψ, thus obtaining a system of n independent equations that can be numerically solved by means of an iterative numerical routine. Note that the number n of selected ψ angles, and thus the number of independent equations, should exceed the number of unknown parameters (i.e., in this case, five unknown parameters: θ_p, φ_p, ψ_p, λ_2 and λ_4). Given the high number of variables involved in the integration, and the large number of collected points in the polyethylene structure, the computation can be quite time consuming (i.e., it required several weeks in our case using *Wolfram Mathematica* software and a commercially available workstation *Dell Precision T7400*). In the interval, $0\le\psi\le\pi/2$ we collected $n=19$ relative intensity values at each investigated location, which largely exceeded the number of unknown parameters. From any five independent equations, we obtained the unknown parameters, θ_p, φ_p, ψ_p, λ_2 and λ_4 according to a best fitting procedure (partial least squares regression method), while using the remaining equations for a confirmation of the obtained values. An additional computational routine is needed for determining the three parameters A, $<P_2(\cos\beta)>$ and $<P_4(\cos\beta)>$. Lagrange multipliers, calculated by the aforementioned fitting procedure, enabled solving a system of three additional equations, as follows (Jaynes, 1957; Pérez et al., 2008):

$$\int_{\gamma=0}^{\gamma=2\pi}\int_{\alpha=0}^{\alpha=2\pi}\int_{\beta=0}^{\beta=\pi} f(\alpha,\beta,\gamma)\sin\beta d\beta d\alpha d\gamma=1 \quad (12)$$

$$\int_{\gamma=0}^{\gamma=2\pi}\int_{\alpha=0}^{\alpha=2\pi}\int_{\beta=0}^{\beta=\pi} P_2(\cos\beta)f(\beta)\sin\beta d\beta d\alpha d\gamma=\langle P_2(\cos\beta)\rangle \quad (13)$$

$$\int_{\gamma=0}^{\gamma=2\pi}\int_{\alpha=0}^{\alpha=2\pi}\int_{\beta=0}^{\beta=\pi} P_4(\cos\beta)f(\beta)\sin\beta d\beta d\alpha d\gamma=\langle P_4(\cos\beta)\rangle \quad (14)$$

from the solution of which the two "order parameters", $<P_2(\cos\beta)>$ and $<P_4(\cos\beta)>$ can be obtained. The parameter

$<P_2(\cos\beta)>$ is also known as Hermans' orientation parameter and can be used to characterize the statistical distribution of the molecular structure. In fact, $<P_2(\cos\beta)>$ assumes the value 0 when the molecular orientation is fully random, while values 1 and –0.5 are experienced when full mole cular alignments parallel and perpendicular to a preferential orientation axis, respectively, are reached. In this study, the calculated value of θ_p represents the out-of plane tilt angle with respect to the uniaxially loaded surface of the polyethylene bearing (cf. Fig. 2a and b). This angle, thus, directly represents the main microstructural modification induced in the polymeric structure by a compressive strain field applied along a direction perpendicular to the bearing surface. Out-of-plane angular displacements should be distinguished from variations of in-plane angle, ψ_p, which, in a previous study (Takahashi et al., 2010), were related to molecular displacements taking place on the surface of the bearings (i.e., at the contact point), owing to the development of frictional forces.

3.3. *Statistical analysis of crystallinity*

Volume fractional assessments of crystalline (α_c) phase employed the relative intensity of vibrational bands located at 1080, 1293 and 1305 cm^{-1} in the vibrational spectrum of polyethylene, as obtained from unpolarized Raman spectra. This spectroscopic method was early proposed by Strobl and Hagedorn (1978) and then refined by Rull et al. (1993). The band located at 1080 cm^{-1} arises from C–C stretching vibrational mode, while the two bands at around 1293 and 1305 cm^{-1} are related to –CH- twisting vibrational modes. These specific vibrational modes are not directly related to long-range 3-D order, but they are related to conformational state populations, which may lead to 3-D crystallinity. Therefore, when a crystallinity fraction is mentioned in the remainder of this work, it shall refer to cumulative conformational populations that might be present in both crystalline and non-crystalline regions of the material. Statistical assessments were obtained by means of the same procedure described above for the assessments of bandwidth (FWHM).

4. Results and discussion

4.1. *Response to externally applied strain of different polymeric structures*

As a first step in the presented characterizations, the microstructures of the two types of investigated UHMWPE have been monitored in their as-received state with respect to their response to a constant state of compressive strain. The material as received from the manufacturer supposedly incorporated some amount of residual strain, as introduced by the manufacturing process. However, not yet being subjected to external load, the as-received sample was conventionally assigned $\varepsilon=0$ and a constant (uniaxial) strain magnitude (i.e., referred to as true strain before recovery, ε_i) was increasingly applied at subsequent steps up to a level $\varepsilon_i=32\%$. Fig. 3(a) shows plots of true strain after recovery, ε_f, as a function of externally applied strain, ε_i, for both Crossfire™ and X3™ materials. In Fig. 3(b) are shown plots of the applied load, P, as a function of strain, ε_i, before recovery, as measured by the load cell at the beginning and at the end of the loading period, namely before and after stress relaxation, respectively. The $\varepsilon_f=\varepsilon_f(\varepsilon_i)$ plots obtained for both materials were linear in nature and their comparison revealed a distinct difference in slope (in inset), which was higher for Crossfire™ as compared to the X3™ material. A comparison between the plots in Fig. 3(a) and (b) showed that, for the same applied constant strain, ε_i, the X3™ material revealed a higher capacity of recovery, thus incorporating a lower amount of plastic strain, ε_f, and internal stress. This experimental finding can be interpreted as a clear proof for a higher resistance to permanent deformation of the X3™ microstructure as compared to that of Crossfire™. A check on the variation of crystallinity upon compressive loading showed no appreciable variation in both materials (Fig. 4), thus confirming that only the initial difference in crystallinity plays a role in the observed difference in deformation behavior between the two investigated materials.

In Fig. 5(a), experimental results are shown of band broadening ($\Delta\omega$=FWHM) as retrieved from unpolarized Raman

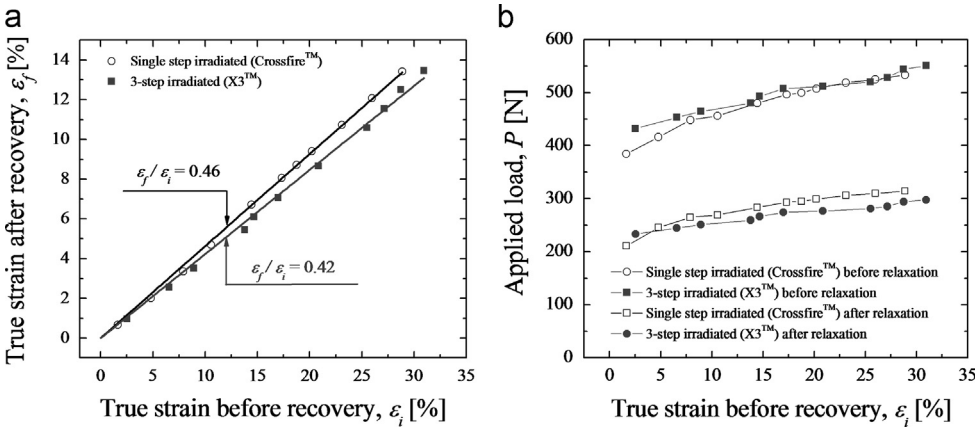

Fig. 3 – (a) Plots of true strain after recovery, ε_f, as a function of externally applied (initial) strain, ε_i, are shown for Crossfire™ and X3™ materials. The slope of the linear plot was higher for the former material, as shown in inset. (b) Plots of applied compressive load versus true strain, ε_i, for the two materials under investigation.

spectra at different values of residual compressive strain, ε_f, after strain recovery. The 1130 cm^{-1} band of the orthorhombic polyethylene structure was narrower in spectra collected from X3™ as compared to Crossfire™ (4.12 vs. 4.47 cm^{-1}), due to the higher crystallinity of the former material (61.7% vs. 58%) (Collier et al., 2003; Wang et al., 2006) and to its higher degree of molecular alignment, as we will explicitly show in the next section, and possibly its lower gradient of residual strain incorporated during processing. All these characteristics were a consequence of the three-step irradiation/annealing process followed in the liner manufacturing. The lower molecular weight of the starting resin of X3™ (GUR1020) as compared to that of Crossfire™ (GUR1050) obviously had also a role in the formation of the recorded spectroscopic difference (Barron and Birkinshaw, 2009). For better distinguishing the repercussions of external strain on microstructural rearrangement from the initial effects of the manufacturing procedures, the trends of band broadening observed in both types of material can be replaced with the bandwidth variation, $\Delta\omega-\Delta\omega_0=\Delta FWHM$, with respect to the initial bandwidth value, $\Delta\omega_0$, in the as-received undeformed state. Accordingly, curves $\varepsilon_f=\varepsilon_f(\Delta FWHM)$ relating the plastic strain after recovery to spectroscopic features could be obtained, as shown in Fig. 5(b). Least-square fitting of the experimental data in Fig. 5(b) led to two phenomenological equations of a common cubic nature, as follows:

$$\varepsilon_f = 18.05\Delta FWHM - 21.04\Delta FWHM^2 + 24.76\Delta FWHM^3 \quad (15)$$

$$\varepsilon_f = 13.11\Delta FWHM - 7.77\Delta FWHM^2 + 24.28\Delta FWHM^3 \quad (16)$$

in which $\Delta FWHM$ is expressed in units of cm^{-1}. Eqs. (15) and (16) refer to X3™ and Crossfire™ liners, respectively. The plots in Fig. 5(b) shows that, under the same level of applied strain, $\varepsilon_i<5\%$, the Raman spectrum of the X3™ material undergoes a relatively lower broadening than that of Crossfire™. Fig. 6(a) and (b) shows examples of experimental angular dependencies of the A_g+B_{1g} Raman mode on the azimuthal rotation angle, ψ, obtained upon in-plane rotation at different stages of uniaxial deformation for the single-step and sequentially irradiated polyethylene structures, respectively. In both cases, with increasing the plastic strain stored in the material, a tendency to follow an angular periodicity of $\pi/2$ rather than π could be noticed, which was clearly a physical consequence of molecular alignment under strain. Numerical least-square fitting of the collected polarized intensities according to Eqs. (10)–(14) enabled us to retrieve the values of preferential tilt angle, θ_p, and Hermans parameter, $<P_2(\cos\beta)>$, which were plotted as a function of increasing plastic strain in Fig. 7(a) and Fig. 8, respectively, for both investigated materials. Upon subtracting the respective initial tilt angles, θ_{p0}, plots of $\varepsilon_f(\theta_p-\theta_{p0})=\varepsilon_f(\Delta\theta_p)$ could be obtained for the two UHMWPE materials, as shown in Fig. 7(b). A comparison between the two plots in Fig. 7(b) clarifies that the X3™ material undergoes a higher tilting

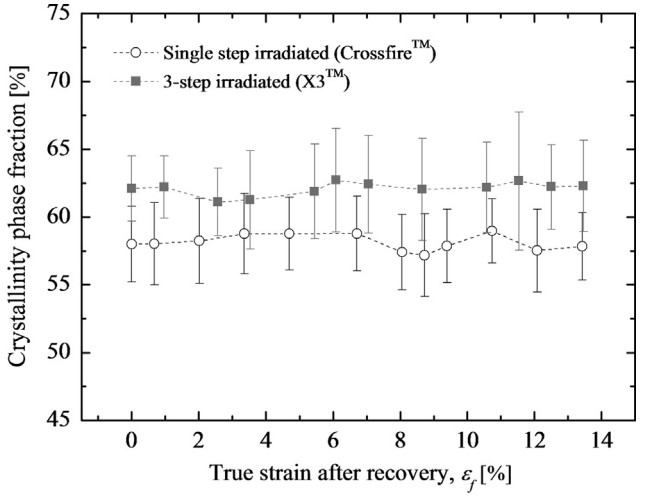

Fig. 4 – Plots of crystallinity variations upon compressive loading. Crystallinity fractions for the two samples in the as-received state were 61.7% and 58% for X3™ and Crossfire™ liners, respectively.

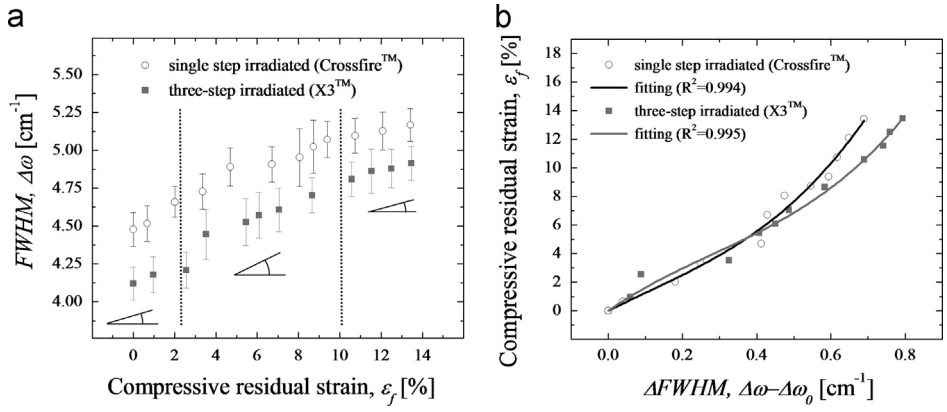

Fig. 5 – (a) Experimental plots of broadening, $\Delta\omega=FWHM$, of the unpolarized 1130 cm^{-1} Raman band as a function of residual plastic strain, ε_f, after recovery are shown for Crossfire™ and X3™ materials. Both plots could be rationalized according to a division into three distinct deformation zones (separated by vertical dotted lines) with different slopes as shown in inset; (b) the experimental dependencies in (a) are re-plotted with taking the respective bandwidth variations with respect to initial bandwidth, $\Delta\omega-\Delta\omega_0=\Delta FWHM$, in abscissa. This procedure enables extracting the effect of applied strain on the Raman band as distinguished from the initial difference arising from the different manufacturing procedures. Least-square fitting curves (correlation coefficients, R^2, in brackets in inset) are analytically represented by Eqs. (15) and (16) for X3™ and Crossfire™ materials, respectively.

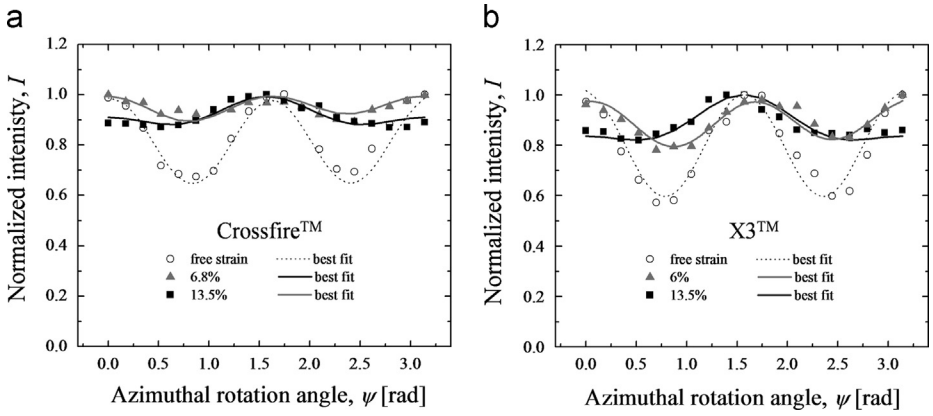

Fig. 6 – Experimental angular dependencies of the A_g+B_{1g} mode Raman intensity on the azimuthal rotation angle, ψ, obtained upon in-plane rotation at different stages of uniaxial deformation for Crossfire™ and X3™ materials (in (a) and (b), respectively).

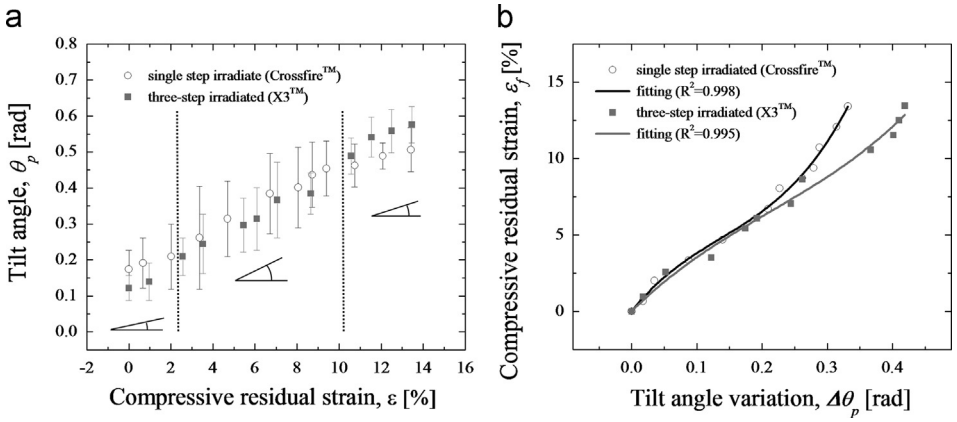

Fig. 7 – (a) Experimental plots of preferential tilt angle, θ_p, as a function of residual plastic strain, ε_f, after recovery are shown for Crossfire™ and X3™ materials. Similar to Fig. 4(a), both plots can be rationalized according to a division into three distinct deformation zones (separated by vertical dotted lines) with different slopes as shown in inset; (b) the experimental dependencies in (a) are re-plotted with taking the tilt angle variation, $\Delta\theta_p=\theta_p-\theta_{p0}$, in abscissa, thus separating the effect of applied strain on tilt angle from the effect of different manufacturing procedures. Least-square fitting curves (correlation coefficients, R^2, in brackets in inset) are analytically represented by Eqs. (17) and (18) for X3™ and Crossfire™ materials, respectively.

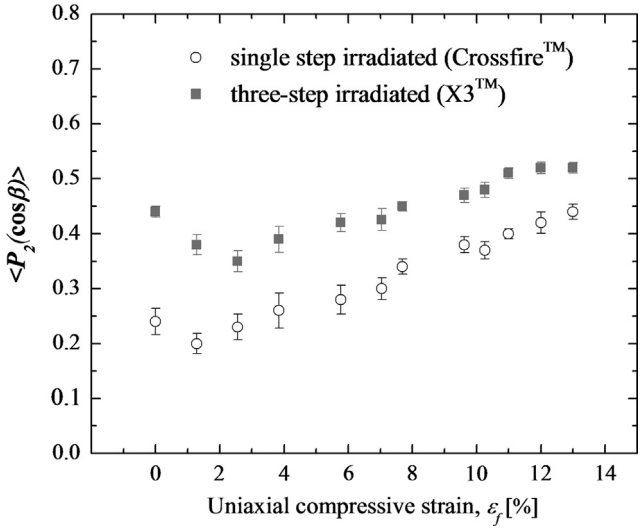

Fig. 8 – Plots of Hermans' parameter, $\overline{\langle P_2(\cos\beta)\rangle}$, as a function of residual plastic strain, ε_f, for both the investigated materials.

rotation at the molecular scale than Crossfire™ for the same magnitude of applied strain, $\varepsilon_f>5\%$. Similar to the case of band broadening analysis, a least-square cubic polynomial fitting suitably applied to the observed experimental trends of molecular rearrangement, leading to the obtainment of two phenomenological curves, $\varepsilon_f=\varepsilon_f(\Delta\theta_p)$, as follows:

$$\varepsilon_f = 53.38\Delta\theta_p - 200.97\Delta\theta_p^2 + 488.32\Delta\theta_p^3 \quad (17)$$

$$\varepsilon_f = 42.45\Delta\theta_p - 83.05\Delta\theta_p^2 + 131.31\Delta\theta_p^3 \quad (18)$$

in which $\Delta\theta_p$ values are expressed in units of radiant. Eqs. (17) and (18) refer to X3™ and Crossfire™ liners, respectively. A clear difference could be found in the $\Delta\theta_p$ trends in the two investigated materials for $\varepsilon_f>5\%$. At high plastic strains, the difference in the variation of out-of-plane tilt angle with respect to its value in original molecular orientation was more marked in the X3™ material, and the origin of such difference will be the object of the discussion given in the next section.

4.2. *Microstructural modifications under strain and their implications on implant functionality*

Based on the salient notions that could be extracted from the plots of Figs. 3, 5, 7 and 8, we can attempt to rationalize the origin of the microstructural modifications induced by uniaxial compression in bulk polyethylene and, ultimately, to discriminate the differences related to the particular processing that the polymer underwent to. Spectroscopic studies of deformation in highly crystalline and textured polymers (e.g., fibers) usually show the occurrence of both Raman band shift and bandwidth broadening, as a consequence of stretching of oriented molecules in both crystalline and amorphous regions (Moonen et al., 1992; Tashiro et al., 1988; Yeh and Young, 1998). Unlike those studies, in our experiment on bulk polyethylene, the observed broadening of the 1130 cm^{-1} band was accompanied by a discernible statistical invariance of peak position (i.e., characterized by scattered values, but conspicuously constant in its average with increasing plastic strain). Spectral shifts of Raman bands under strain are expected to occur toward opposite directions for applied (uniaxial) strain magnitudes of tensile and compressive nature. The Raman band is also expected to only broaden (without shifting), when both types of deformation events (i.e., tensile and compressive) occur with the same statistical relevance at different locations within the probe volume. We have indeed already noticed in a previous study the tendency to band broadening without shifting under increasing plastic strain in biomedical polyethylene (Kumakura et al., 2009). We take a further step in the present systematic investigation of plastic deformation processes, and aim at rationalizing the molecular behavior by invoking a three-stage model, which could explain the sequence of microstructural modifications induced by uniaxial compressive load on the polymeric structure. The sigmoidal shape of the experimental curves in Figs. 5 and 7(a), which can be fitted to three distinct linear segments with different slopes, indeed suggests the existence of three stages in the overall deformation process. According to general notions in the field of deformation of bulk polymers (Lin and Argon, 1994; Bartczak et al., 1992), the inelastic response of semicrystalline UHMWPE can be considered to begin with the main deformation process occurring within the amorphous regions of the polymeric structure, immediately followed by the activation of plastic deformation into the crystalline lamellae, predominantly via crystallographic slip mechanisms. Fig. 9(a) shows a schematic representing the microstructure of undeformed polyethylene, in which, according to our measurements of tilt angle (cf. Fig. 7a), the preferential orientation of lamellar axes is broadly perpendicular to the bearing surface of the liners for both single-step and sequentially irradiated UHMWPE samples. This finding is in agreement with a previous study by Bellare and Cohen (1996), who determined the nature of crystallographic texture in the bulk of ram-extruded rods and compression-molded sheets of UHMWPE. Both processing procedures indeed induced crystallographic texture in the polymer microstructures, although the compression-molded sheets employed for manufacturing X3™ displayed a higher degree of orientation, as revealed by the higher value of the Hermans parameter in Fig. 8 (i.e., at ε_f). The preferential orientation of molecular chains is a consequence of crystallization of the oriented polyethylene melt under a perpendicular compressive stress. In the amorphous phase surrounding the crystalline orthorhombic lamellae, due to the high molecular weight of polyethylene and to the high irradiation dose applied, the concentration of

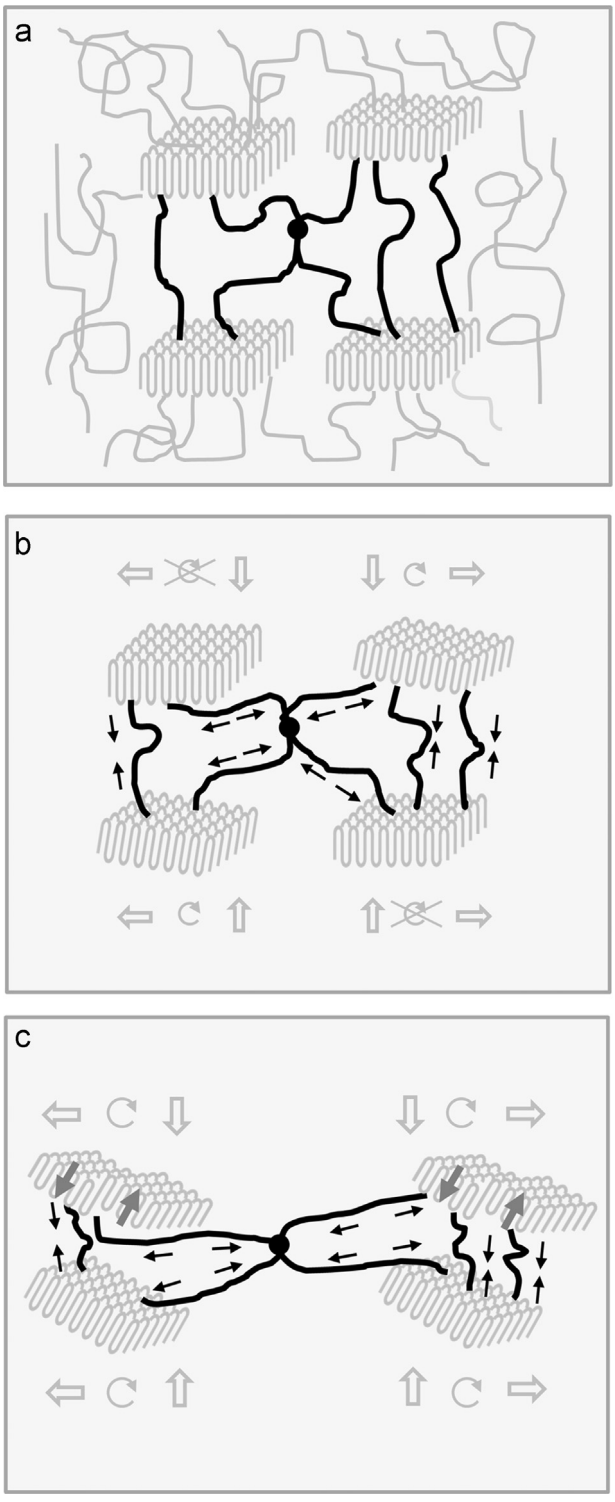

Fig. 9 – Schematics explaining the local development of both compressive and tensile strain gradients upon application of compressive external load on the composite (amorphous/crystalline) structure of UHMWPE ((a) unloaded, (b) and (c) at increasing levels of external strain). The local presence of both types of strain gradient leads to the observed (and calibrated) Raman band broadening (cf. Fig. 4).

tie molecules, entanglements and crosslinks is high and affects the response of the microstructure to the applied external load. During the first stage of deformation (i.e., up to ≈2% plastic strain, as shown in Figs. 5 and 7(a)), the molecular chains present in the amorphous phase are those mainly undergoing deformation. However, the important characteristic since the initial stage of deformation is that the strain locally stored in the structure is not necessarily compressive in nature, due to the high concentration of entanglements and crosslinks throughout the disordered (amorphous) phase (cf. Fig. 9b). At this initial stage, rotation of crystalline lamellae is barely activated by the external compressive load, as demonstrated by only a slight increase of the tilt angle, θ_p (cf. Fig. 7a). The decrease of Hermans' parameter during the initial deformation stage, consistently recorded for both the investigated materials (cf. Fig. 8), rather suggests the development of a igher state of disorder in the structure. The increasing presence of strain gradients within the probe volume, especially in the amorphous fraction of the materials, explains the incipient occurrence of band broadening (as shown in Fig. 5 (a)). During the stage of secondary deformation (i.e., in the range $2 \leq \varepsilon_f \leq 11\%$; cf. Figs. 5 and 7(a)), both materials showed the most remarkable variations in θ_f and $\Delta FWHM$. Significant band broadening, due to over stressed tie molecules, entanglements and crosslinks between crystalline and amorphous regions, arose from steeper strain gradients of both tensile and compressive nature (Fig. 9(c)). Moreover, as shown by the pronounced rising of the $<P_2 (\cos \beta)>$ parameter (cf. Fig. 8), crystalline lamellae underwent significant rotation in this secondary stage of deformation, with a larger population of crystallites experiencing preferential orientation and aligning along a plane parallel to the sample surface. The rotation of lamellae should be massively activated by the previously mentioned exacerbation of tensile and compressive strain gradients in the amorphous phase (cf. Fig. 9c), while also a mechanism of structural re-arrangement of intra-lamellar sliding concurrently takes place on the crystalline side of the structure (Galeski et al., 1992). By comparing the secondary stage of deformation as occurring in the two different liners, we have already noticed that the increase in tilt angle starts to be more pronounced in X3™ than in Crossfire™. This finding indirectly confirms the higher concentration of crosslinks in the amorphous phase of the former material, although the cumulative dose of irradiation was the same for both materials. In fact, as proved by Bartczak (2010) and Boontongkong et al. (1998), when subjected to the same strain magnitude in a range of relatively low deformations, highly entangled and/or highly cross-linked polyethylene structures achieve a higher degree of crystallographic orientation as compared to less cross-linked and/or less entangled structures. In other words, if the concentration of crosslinking is high, the molecular chains in the amorphous region might quickly become fully stretched to their maximum limit, i.e., even at relatively low strain magnitudes. Such microstructural circumstance in turn triggers a faster reorientation of the crystalline lamellae according to the mechanism shown in Fig. 9. In the last (third) stage of compressive deformation (i.e., true strains in the interval, $11 \leq \varepsilon_f \leq 13\%$), the observed variations of bandwidth and molecular orientation became milder than those in the second deformation stage (cf. lower slopes in Figs. 5 and 6(a)). Such a mitigation of the process of molecular rearrangement concurs with the saturation of the rotation process, with a large population of molecular chains now experiencing preferential orientation at maximized tilt angle variations, $\Delta\theta_p$. Further plastic flow among crystalline lamellae is hampered by the onset of strain hardening correlated to the presence of crosslinks. Above this stage, only chain slip within individual crystallites can be expected to become active as an intrinsic deformation mechanism. Crystalline slip occurs along the [001] direction of the orthorhombic structure (i.e., which corresponds to slip along the most closely packed crystallographic plane) (Galeski et al., 1992). In other words, strain hardening becomes the preponderant effect and should also be responsible for the milder band broadening shown by both materials in Fig. 5(a) at $\varepsilon_f \geq 11\%$. Such high levels of plastic strain, however, are not expected to occur under the mere effect of creep deformation in acetabular cups. On the other hand, the severe damage induced by abrasive/adhesive wear might locally produce extreme elongations in the lamellae, with the microstructure developing a texture similar to that of a single crystal (fibrillar structure) (Galeski et al., 1992). At these extreme levels of deformation, the effect of strain hardening induced by crosslinking should also be maximized. At the compressive strain levels experienced by the two investigated materials during the present characterization of plastic deformation, we could only detect to a lower extent the difference in strain hardening effect between X3™ and Crossfire™ materials. Nevertheless, it was clarified that sequentially irradiated UHMWPE, despite being produced from a lower molecular weight resin (i.e., with an expectedly lower initial concentration of molecular entanglements), showed a higher resistance to plastic deformation and a larger recovering capacity, and underwent to a faster molecular orientation at the initial deformation stage (i.e., up to 11% compressive plastic strain) as compared to single-step irradiated polyethylene. Such properties, which should also involve an earlier strain hardening effect at higher strain levels, are representative of an improvement in deformation behavior as a consequence of the sequentially applied irradiation/annealing manufacturing procedure.

4.3. *Analyses of microstructural modifications in short-term retrievals*

As an applicative demonstration of the Raman spectroscopic assessments shown in Section 4.1, two retrieved hip cups were analyzed in order to compare the short-term *in vivo* response of Crossfire™ and X3™ components. The shown results, despite lacking statistical validity for the availability of only one cup for each type of material, might provide confirmation of the creep deformation behavior *in vivo* and represent a tangible demonstration of the effectiveness of the developed Raman spectroscopic technique. Fig. 10 shows the results collected on Retrieval #1 (Crossfire™). In (a), a histogram of residual (plastic) strain is given as calculated from Raman bandwidth data according to Eq. (16), which was retrieved at a fixed location 50 μm below the surface of the main wear zone; and, in (c), the results of Raman intensity variation upon in-plane rotation at the same subsurface location with the determination of the average tilt angle of the molecular chains, its average variation with respect to the molecular arrangement in the as-received cup, and the average Hermans parameter in the main wear zone (all parameters shown in inset in Fig. 10(c)). In Fig. 10(b) and (d), similar results are presented for Retrieval #2 (X3™). Comparing the histograms

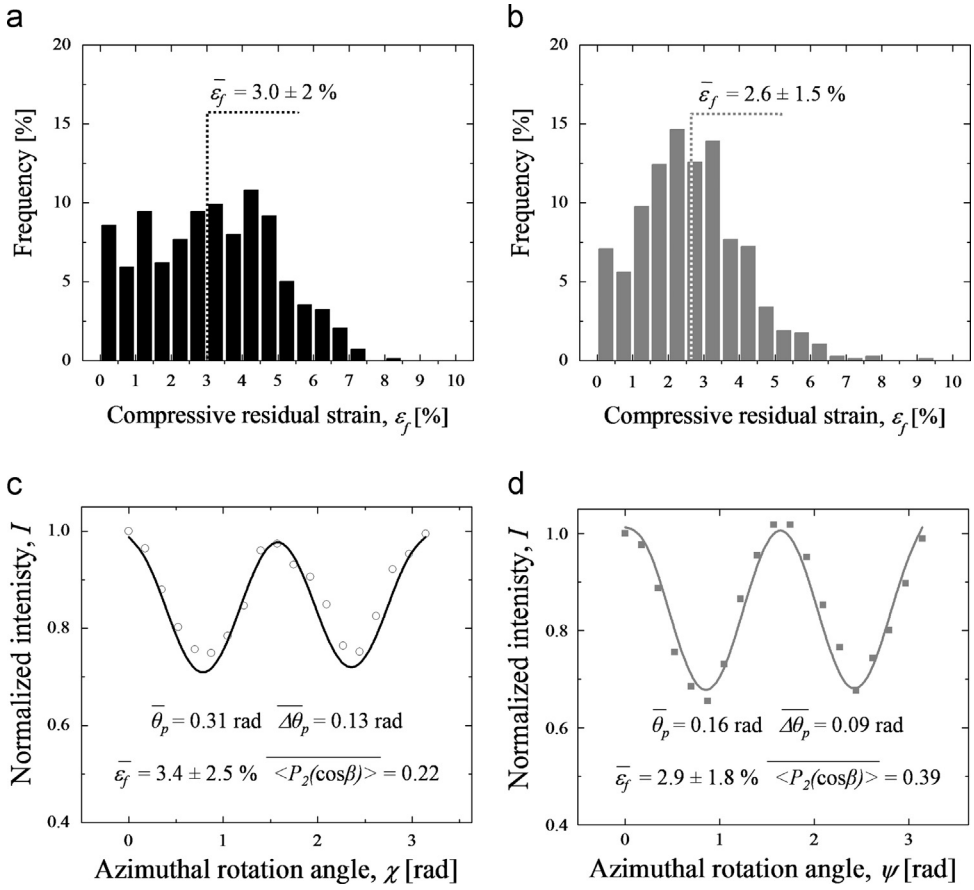

Fig. 10 – In (a) and (b), histograms of residual (plastic) strain, ε_f, as statistically retrieved from Raman bandwidth data, $\Delta FWHM$, in the main wear zone of the Crossfire™ and X3™ short-term retrievals. (c) and (d) shows Raman intensity variations upon in-plane probe rotation in the main wear zone of the Crossfire™ and X3™ short-term retrievals, respectively. Azimuthal angle rotation results were used for the determinations of average tilt angles, $\bar{\theta}_p$, and average tilt angle variations, $\overline{\Delta\theta_p}$, of the molecular chains, and average Hermans parameter, $\overline{\langle P_2(\cos\beta)\rangle}$ (all parameters shown in inset together with the average plastic strain, $\bar{\varepsilon}_f$, obtained from the histograms in (a) and (b)).

in Fig. 10(a) and (b), one could notice a 21% lower average plastic strain, $\bar{\varepsilon}_f$, and a less broad strain distribution in the X3™ liner as compared to the Crossfire™ liner. The lower average strain could also be related to the shorter implantation time of Retrieval #2 (cf. Table 2), while the sharper distribution is a clear consequence of a more homogeneous microstructure both in terms of crystallinity and molecular alignment. The value obtained for the average tilt angle in the X3™ liner was about half that found in the Crossfire™ one ($\bar{\theta}_p = 0.16$ vs. 0.31 rad; cf. inset values in Fig. 10(c) and (d), respectively), consistent with the initial difference in molecular alignment in the as-received cups (cf. Fig. 7(a)). Very low variations in tilt angle, $\overline{\Delta\theta_p}$, were detected in both retrievals, while the average value of Hermans parameter, $<P_2(\cos\beta)>$, was discernibly higher in the X3™ retrieval as found for the unused cups. These characteristics confirm that both the *in vivo* exposed UHMWPE structures were yet in their quite early stages of plastic deformation. Interestingly, the average tilt angles found in both retrievals were slightly higher than those obtained *in vitro* for the same amount of plastic strain. This is probably due to the influence of frictional sliding on molecular assembly, which, unavailable in static tests conducted *in vitro*, might promote some additional effect on the rotation of lamellae also in the material subsurface. According to the shown results, after few months of *in vivo* implantation, the two retrievals experienced comparably low levels of creep strain and quite low variations in rotation angles of molecular chains towards directions perpendicular to that of applied load.

5. Conclusion

In this study, phenomenological correlations enabling non-destructively assessments of residual compressive strain in polyethylene hip cups by Raman spectroscopy have explicitly been determined for two UHMWPE materials belonging to two successive design generations of gamma-irradiated materials. Polarized Raman spectroscopy was also applied to retrieve variations in tilt angle occurring upon loading and representing the main microstructural rearrangement occurring during creep deformation. The material manufactured by sequentially applied irradiation/annealing steps was more resistant to plastic deformation than the one irradiated with the same dose and annealed by a single-step procedure. Based on the calibration results collected *in vitro* on the as-received

materials, quantitative analyses were also conducted of the plastic compressive strain generated in the main wear zone during short-term *in vivo* loading. A comparison between retrievals made of single-step and sequentially irradiated liners revealed comparably low levels of creep strain and quite low amounts of tilting rotation of molecular chains under body weight.

REFERENCES

Barron, D., Birkinshaw, C., 2009. On the morphology of some irradiated ultra high molecular weight polyethylenes. Polymer Degradation and Stability 94, 1621–1631.

Bartczak, Z., 2010. Effect of chain entanglements on plastic deformation behavior of ultra-high molecular weight polyethylene. Journal of Polymer Science Part B: Polymer Physics 48, 276–285.

Bartczak, Z., Argon, A.S., Cohen, R.E., 1992. Deformation mechanisms and plastic resistance in single-crystal-textured high-density polyethylene. Macromolecules 25, 5036–5053.

Bartczak, Z., Cohen, R.E., Argon, A.S., 1992b. Evolution of the crystalline texture of high-density polyethylene during uniaxial compression. Macromolecules 25, 4692–4704.

Bellare, A., Cohen, R.E., 1996. Morphology of rod stock and compression-moulded sheets of ultra-high-molecular-weight polyethylene used in orthopaedic implants. Biomater 17, 2325–2333.

Boontongkong, Y., Cohen, R.E., Spector, M., Bellare, A., 1998. Orientation of plane strain-compressed ultra-high-molecular-weight polyethylene. Polymer 39, 6391–6400.

Citra, M.J., Chase, D.B., Ikeda, R.M., Gardner, K.H., 1995. Molecular orientation of high-density polyethylene fibers characterized by polarized Raman spectroscopy. Macromolecules 28, 4007–4012.

Collier, J.P., Currier, B.H., Kennedy, F.E., Currier, J.H., Timmins, G. S., Jackson, S.K., Brewer, R.L., 2003. Comparison of cross-linked polyethylene materials for orthopaedic applications. Clinical Orthopaedics and Related Research 414, 289–304.

Dai, X., Omori, H., Okumura, Y., Ando, M., Oki, H., Hashimoto, N., Baba, H., 2000. Serial measurement of polyethylene wear of well-fixed cementless metal-backed acetabular component in total hip arthroplasty: an over 10 year follow-up study. Artificial Organ 24, 746–751.

Devane, P.A., Horne, J.G., 1999. Assessment of polyethylene wear in total hip replacement. Clinical Orthopaedics and Related Research 369, 59–72.

Dumbleton, J.H., Manley, T., Edidin, A.A., 2002. A literature review of the association between wear rate and osteolysis in total hip arthroplasty. Journal of Arthroplasty 17, 649–661.

Galeski, A., Bartczak, Z., Argon, A.S., Cohen, R.E., 1992. Morphological alterations during texture-producing plastic plane strain compression of high-density polyethylene. Macromolecules 25, 5705–5718.

Grobbelaar, C.J., du Plessis, T.A., Marais, F., 1978. The radiation improvement of polyethylene prostheses. A preliminary study. Journal of Bone and Joint Surgery 60-B, 370–374.

Haraguchi, K., Sugano, N., Nishii, T., Sakai, T., Yoshikawa, H., Ohzono, T., 2001. Influence of polyethylene and femoral head surface quality on wear: a retrieval study. International Orthopaedics 25, 29–34.

Isaac, G.H., Dowson, D., Wroblewski, B.M., 1996. An investigation into the origins of time-dependent variation in penetration rates with Charnley acetabular cups-wear, creep or degradation?. Proceedings of the Institution of Mechanical Engineers, Part H 210, 209–216.

James, S.P., Blazka, S., Merrill, E.W., Jasty, M., Lee, K.R., Bragdon, C. R., Harris, W.H., 1993. Challenge to the concept that UHMWPE acetabular components oxidize in vivo. Biomaterials 14, 643–647.

Jaynes, E.T., 1957. Information theory and statistical mechanics. Physical Review 106, 620–630.

Kumakura, T., Puppulin, L., Yamamoto, K., Takahashi, Y., Pezzotti, G., 2009. In-depth oxidation and strain profiles in UHMWPE acetabular cups non-destructively studied by confocal Raman microprobe spectroscopy. Journal of Biomaterials Science, Polymer Edition 20, 1809–1822.

Lin, L., Argon, A.S., 1994. Review structure and plastic deformation of polyethylene. Journal of Materials Science 29, 294–323.

Loudon, R., 1964. The Raman effect in crystals. Advances in Physics 13, 423–482.

Maxian, T.A., Brown, T.D., Pedersen, D.R., Callaghan, J.J., 1996a. A sliding distance-coupled finite element formulation for polyethylene wear in total hip arthroplasty. Journal of Biomechanics 29, 687–692.

Maxian, T.A., Brown, T.D., Pedersen, D.R., Callaghan, JJ., 1996b. 3-Dimensional sliding/contact computational simulation of total hip wear. Clinical Orthopaedics Related Research 333, 41–50.

McDonald, M.D., Bloebaum, R.D., 1995. Distinguishing wear and creep in clinically retrieved polyethylene inserts. Journal of Biomedical Materials Research 29, 1–7.

McKellop, H., Shen, F., Lu, B., Campbell, P., Salovey, R., 1999. Development of an extremely wear-resistant ultra high molecular weight polyethylene for total hip replacement. Journal of Orthopaedic Research 17, 157–167.

Meyer, R.W., Pruitt, L.A., 2001. The effect of cyclic true strain on the morphology, structure, and relaxation behavior of ultra high molecular weight polyethylene. Polymer 42, 5293–5306.

Moonen, J.A.H.M., Roovers, W.A.C., Meier, R.J., Kip, B.J., 1992. Crystal and molecular deformation in strained high-performance polyethylene fibers studied by wide-angle X-ray scattering and Raman spectroscopy. Journal of Polymer Science Part B: Polymer Physics 30, 361–372.

Moratoglu, O.K., Bragdon, C.R., O'Connor, D.O., Jasty, M., Harris, W.H., Gul, R., 1999. Unified wear model for highly crosslinked ultra-high molecular weight polyethylenes (UHMWPE). Biomaterials 20, 1463–1470.

Moratoglu, O.K., Bragdon, C.R., O'Connor, D.O., Jasty, M., Harris, W.H., 2001. A new method of crosslinking UHMWPE to improve wear, reduce oxidation and retain mechanical properties. Journal of Arthroplasty 16, 149–160.

Morscher, E.W., Dick, W., Kernen, V., 1982. Cementless fixation of polyethylene acetabular component in total hip arthroplasty. Archives of Orthopaedic and Trauma Surgery 99, 223–230.

Nikolaeva, G.Y., Semenova, L.E., Prokhorov, K.A., Gordeyev, S.A., 1997. Quantitative characterization of macromolecules orientation in polymers by micro Raman spectroscopy. Laser Physics 7, 403–415.

Oonishii, H., Kadoya, Y., 2000. Wear of high-dose gamma-irradiated polyethylene in total hip replacement. Journal of Orthopaedic Science 5, 223–228.

Oparaugo, P.C., Clarke, I.C., Malchau, H., Herberts, P., 2001. Correlation of wear debris-induced osteolysis and revision with volumetric wear-rates of polyethylene: A survey of 8 reports in the literature. Acta Orthopaedica 72, 22–28.

Pedersen, D.R., Callaghan, J.J., Johnston, T.L., Fetzer., G.B., Johnston, R.C., 2001. Comparison of femoral head penetration rates between cementless acetabular components with 22-mm and 28-mm heads. Journal of Arthroplasty 16, 111–115.

Pérez, R., Banda, S., Ounaies, Z., 2008. Determination of the orientation distribution function in aligned single wall

nanotube polymer nanocomposites by polarized Raman spectroscopy. Journal of Applied Physics 103 074302-1-9.
Pezzotti, G., Kumakura, T., Yamada, K., Tateiwa, T., Puppulin, L., Zhu, W., Yamamoto, K., 2007. Confocal Raman spectroscopic analysis of cross-linked ultra-high molecular weight polyethylene for application in artificial hip joints. Journal of Biomedical Optics 12, 014011 011.
Pezzotti, G., Takahashi, Y., Takamatsu, Y., Puppulin, L., Nishii, T., Miki, H., Sugano, N., 2011. Non-destructively differentiating the roles of creep, wear and oxidation in long-term in vivo exposed polyethylene cups. Journal of Biomaterials Science, Polymer Edition 22, 2165–2184.
Pigeon, M., Prud'homme, R.E., Pézolet, M., 1991. Characterization of molecular orientation in polyethylene by Raman spectroscopy. Macromolecules 24, 5687–5694.
Porto, S.P., Krishnan, R.S., 1967. Raman effect of corundum. Journal of Chemical Physics 47, 1009–1012.
Puppulin, L., Takahashi, Y., Zhu, W., Pezzotti, G., 2011a. Raman polarization analysis of highly crystalline polyethylene fiber. Journal of Raman Spectroscopy 42, 482–487.
Puppulin, L., Takahashi, Y., Zhu, W., Sugano, N., Pezzotti, G., 2011b. Polarized Raman analysis of molecular rearrangement and residual strain on the surface of retrieved polyethylene tibial plates. Acta Biomaterialia 7, 1150–1159.
Roe, R.J., 1964. Orientation distribution function of statistical segments in deformed polymer networks. Journal of Applied Physics 35, 2215–2219.
Rull, F., Prieto, A.C., Casado, J.M., Sobron, F., Edwards, H.G.M., 1993. Estimation of crystallinity in polyethylene by Raman spectroscopy. Journal of Raman Spectroscopy 24, 545–550.
Strobl, G.R., Hagedorn, W., 1978. Raman spectroscopic method for determining the crystallinity of polyethylene. Journal of Polymer Science Part B: Polymer Physics 16, 1181–1193.
Sychterz, C.J., Engh, C.A., Yang, A., Engh, C.A., 1999. Analysis of temporal wear patterns of porous-coated acetabular components: distinguishing between true wear and so-called bedding-in. Journal of Bone and Joint Surgery 81, 821–830.
Takahashi, Y., Puppulin, L., Zhu, W., Pezzotti, G., 2010. Raman tensor analysis of ultra-high molecular weight polyethylene and its application to study retrieved hip joint components. Acta Biomaterialia 6, 3583–3594.
Tashiro, K., Wu, G., Kobayashi, M., 1988. Morphological effect on the Raman frequency shift induced by tensile stress applied to crystalline polyoxymethylene and polyethylene: spectroscopic support for the idea of an inhomogeneous stress distribution in polymer material. Polymer 29, 1768–1778.
Teoh, S.H., Chan, W.H., Thampuran, R., 2002. An elasto-plastic finite element model for polyethylene wear in total hip arthroplasty. Journal of Biomechanics 35, 323–330.
Turrell, G., 1989. The Raman effect. In: Gardiner, D.J., Graves, P.R. (Eds.), Practical Raman Spectroscopy. Springer, Berlin, pp. 1–23.
Wang, A., Stark, C., Dumbleton, J.H., 1996. Mechanistic and morphological origins of ultra-high molecular weight polyethylene wear debris in total joint replacement prostheses. Proceedings of the Institution of Mechanical Engineers, Part H 210, 141–155.
Wang, A., Zeng, H., Yau, S.S., Essner, A., Manely, M., Dumbleton, J., 2006. Wear, oxidation and mechanical properties of a sequentially irradiated and annealed UHMWPE in total joint replacement. Journal of Physics D: Applied Physics 39, 3213–3219.
Wroblewski, B.M., Siney, P.D., Dowson, D., Collins, S.N., 1996. Prospective clinical and joint simulator studies of a new total hip arthroplasty using alumina ceramic heads and cross-linked polyethylene cups. Journal of Bone & Joint Surgery (British Volume) 78, 280–285.
Yang, W., Chen, M.X., 2001. Modeling of large plastic deformation in crystalline polymers. Journal of the Mechanics and Physics of Solids 49, 2719–2736.
Yeh, W.Y., Young, R.J., 1998. Deformation processes in poly (ethylene terephthalate) fibers. Journal of Macromolecular Science: Physics B37, 83–118.
Zhu, Y.H., Chiu, K.Y., Tang, W.M., 2001. Review article: polyethylene wear and osteolysis in total hip arthroplasty. Journal of Orthopaedic Surgery 9, 91–99.